The Momentum Budget and Temporal Evolution of a Mesoscale Convective System

FREDERICK SANDERS AND KERRY A. EMANUEL

Department of Meteorology, Massachusetts Institute of Technology, Cambridge 02139

(Manuscript received 21 June 1976, in revised form 3 November 1976)

ABSTRACT

The momentum budget and temporal evolution of a convective mesosystem, originally investigated by Sanders and Paine (1975), are examined. It is found that 1) alternative analyses of the data do not substantially change the conclusions reached in the previous paper, 2) stresses due to cumulus-scale eddies produce forces which are as large as the horizontal pressure-gradient force, in the direction normal to the storm line, and 3) liquid water aloft must be taken into account in the hydrostatic computation of the pressure field. The mesoscale circulation increases substantially during the 4 h observation period, suggesting a time evolution which may be characteristic of this type of convective system.

1. Introduction

The thermodynamic and hydrologic behavior of a singularly well-observed convective storm in Oklahoma has been described by Sanders and Paine (1975), hereafter referred to as SP. Here we wish to show that the main conclusions are not affected by alternative methods of analyzing the data, provided by the National Severe Storms Laboratory (NSSL), and to present the results of a study of the horizontal momentum in a direction normal to the line of convective storms. In addition we shall consider some aspects of the nonsteady character of the system.

2. Alternative analyses

Taking advantage of the obvious slab symmetry of the radar depiction and of the character of the frontal wind shift as it progressed through the NSSL surface mesonetwork, SP placed each piece of rawinsonde information in one of seven "time blocks," on the basis of its position in time relative to the surface wind shift (SWS). An equivalence between time and distance along the (transverse) y axis was obtained from the mean speed of advance of the SWS. The analysis of the rawinsonde data was based on time-block averages which were crudely corrected for the difference in mean local time between the observations in one time block compared to another. In the absence of such a correction, any temporal trend in a coordinate system moving with the SWS could appear as a spurious spatial variation in the y direction. The vertical motion in a (y,p) cross section, as originally obtained by SP, is shown in Fig. 1a.

The strong mesoscale doublet of ascent and descent which dominates this picture, closely related to the field of v component through the equation of continuity, plays a crucial role in the physical diagnosis of the entire system. Hence we are interested to see how it might be influenced by other equally defensible treatments of the original data.

The first alternative analysis is based on the establishment of temporal trends for each of the two horizontal wind components, the balloon ascent rates, the potential temperature and the mixing ratio, for each 50 mb layer within each time block. These trends, obtained by linear regression, permitted each piece of data to be adjusted to 2000 CST. The vertical motion pattern computed via the kinematic method, from the analysis of the adjusted v component, is shown in Fig. 1b. (The values of $\partial\bar{u}/\partial x$, in the SP analysis, were found to be small compared to the values of $\partial\bar{v}/\partial y$ and were neglected here.) The field of the v component, together with the v-ω streamfunction corresponding to Fig. 1b, appears in Fig. 2. The mesoscale doublet of ascent and descent is still present in about the same location, the ascent about equally strong and the descent distinctly weaker than in the original version. The centers of updraft and downdraft are now somewhat closer together and the mesoscale updraft center now appears slightly earlier than the maximum precipitation observed at the ground (cf. SP, Fig. 14), a physically more pleasing result.

The secondary region of enhanced ascent in the upper left corner of Fig. 1b is probably spurious, since it is the consequence of linear extrapolation of a strong trend beyond the times of the data set for this block, all relevant observations being made after 2000 CST. This trend, though apparently falsifying the 2000 CST picture, is important, and will be discussed later.

In another method of analysis, aimed at producing greater resolution of the motion field in the y direction, the data were plotted for each pressure layer in the x-y plane, with the y distance determined as in SP and the x distance measured from an axis through the NSSL radar site and normal to the SWS. The u and v components were obtained at a rectangular set of grid points with mesh length 5 km, and the results averaged in x with no time correction. In this method the weight attributed to each observation depends in effect on its distance from its neighbors in the x direction, whereas in the time-block averages all observations are weighted equally. The kinematic pattern of vertical motion in the (y,p) plane appears in Fig. 1c. The result strongly resembles the pattern shown in Fig. 1b except in the upper left corner. Both of these versions show that little strong descent occurs ahead of the SWS, and thus avoid most of the physically questionable apparent sink of equivalent potential temperature aloft in this region discussed by SP.

Most importantly, all three analyses confirm the presence of a strong mesoscale downdraft immediately ahead of the main line of radar echoes. We have found a similar structure in an analysis of the Oklahoma squall line of 26 April 1969, which we plan to report in the near future. Moreover, Fankhauser's (1974) analysis of the NSSL data for the squall line of 8 June 1966, showed a similar, though weaker, feature. We tentatively conclude that such a pronounced doublet of mesoscale vertical motion is a characteristic feature of large convective storms, whether of frontal or squall-line character, at this "early mature" stage of their life history.

In all three analyses there is a large and irreconcilable discrepancy between the vertical motions computed from the observed horizontal wind components and those obtained directly from the ascent rates of the balloons. In effect, one must choose whether to accept the horizontal motions or the vertical motions of the balloons. For reasons discussed by SP, we accept the former and thus necessarily find that the balloons tend to seek the updrafts in the presence of active convection, thus giving a biased estimate of the mesoscale mean.

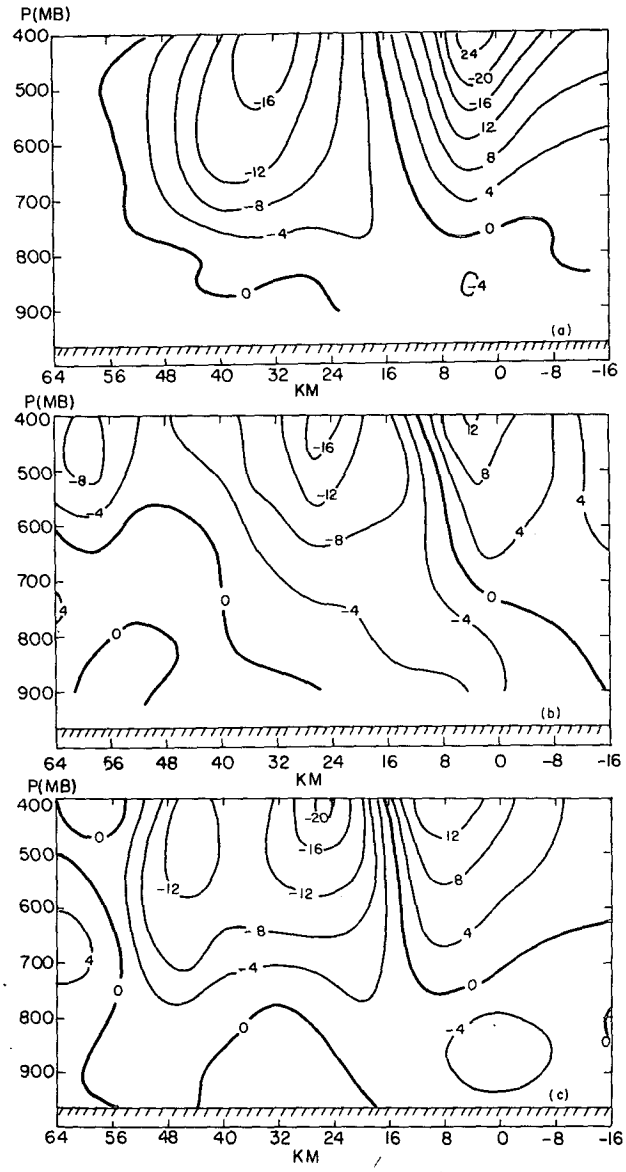

FIG. 1. Alternative kinematic computations of the mesoscale vertical motion $\bar{\omega}$ (see text). Isopleths are at intervals of 4×10^{-2} mb s^{-1}. Zero on the abscissa represents the position of the surface wind shift.

3. The momentum budget

Upon neglect of the effects of variations of motion in the x direction, which seems eminently justifiable in this case, the equation of motion in the y direction can be written

$$\frac{\partial\bar{v}}{\partial t}+\bar{v}\frac{\partial\bar{v}}{\partial y}+\bar{\omega}\frac{\partial\bar{v}}{\partial p}=-\frac{\partial\Phi}{\partial y}-f\bar{u}-\frac{\partial}{\partial y}\overline{(v'v')}-\frac{\partial}{\partial p}\overline{(\omega'v')}, \quad (1)$$

where Φ is the geopotential on a constant pressure surface, the overbar represents the mesoscale mean value, as defined by SP, and the prime represents the departure of the point value from it. We shall apply this equation to the analysis illustrated in Fig. 1b. The left side, the acceleration following the mesoscale motion, can be evaluated directly from the analyses of v and ω as can the second (Coriolis) force on the right side.

The third and fourth terms on the right side, representing forces arising from surface friction and from internal turbulent stresses (mainly convective) can be dealt with, heuristically at least, by taking the individual balloon measurements as an adequate sample of the point values, corrected for the bias dis-

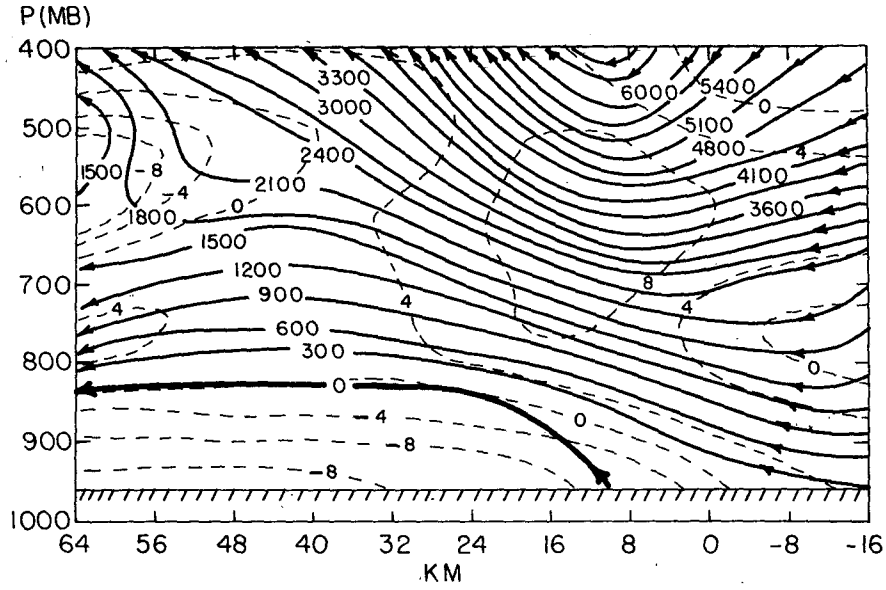

FIG. 2. Analysis of horizontal component v of mesoscale flow (dashed) normal to the surface wind-shift line, at intervals of 4 m s^{-1}, relative to earth; and analysis of streamfunction (solid) of flow in the (y,p) plane, relative to the wind-shift line, at intervals of 300 mb m s^{-1}.

cussed earlier. This correction is made by (somewhat arbitrarily) dividing the computed fluxes, $\overline{v'v'}$ and $\overline{\omega'v'}$ by 2. A simplistic analysis shows that this reduction is roughly equivalent to assuming that the actual percentage of the 10 km mesoscale area element occupied by active convective updrafts is around 10%, rather than the values as high as 60% found in the balloon samples for some time blocks and levels.

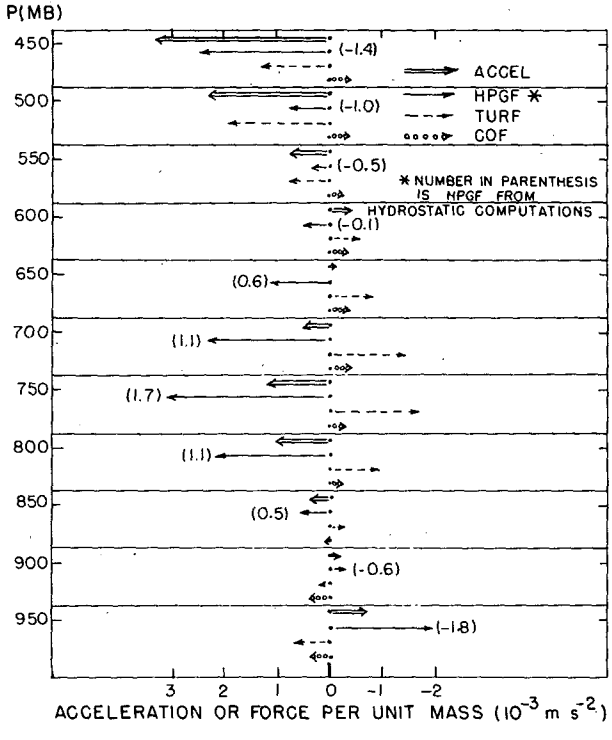

FIG. 3. Acceleration and forces per unit mass in the direction normal to the wind-shift line from $y=-12$ km to $y=60$ km. HPGF is horizontal pressure-gradient force, TURF the turbulent force and COF the Coriolis force.

In the lowest layer, mainly in the well-mixed colder air below the frontal zone, there is no evidence of penetration of convective activity from aloft. Here we have parameterized the surface friction force as $c_D H^{-1}\bar{v}(\bar{u}^2+\bar{v}^2)^{\frac{1}{2}}$, c_D being a drag coefficient of 2×10^{-3} and H a nominal layer depth of 200 m.

With all other terms measured, the horizontal pressure-gradient force per unit mass, $-\partial\Phi/\partial y$, can be obtained as a residual, and the resulting horizontal profile of geopotential can be constructed by integration in y across the domain for each pressure layer. This estimate of the geopotential field can then be compared with an independent estimate obtained hydrostatically from the radiosonde data, as a check on the reliability of the entire analysis.

The v momentum budget for the domain, represented by the integral of (1) from 12 km ahead (roughly southeast) to 60 km to the rear (approximately northwest) of the SWS is shown for each pressure layer in Fig. 3. The horizontal pressure-gradient force shown graphically is the one obtained as a residual, while the corresponding value from the hydrostatic calculation is shown numerically.

In Fig. 3 we see in the lowest layer that the mesoscale parcel acceleration is southeastward, due to the excess of pressure-gradient force over the opposed friction and Coriolis forces. Forces and accelerations are small in the next two layers, containing the frontal

zone and the base of the active convective zone. Between 825 and 675 mb there are large northwestward-directed pressure-gradient forces, opposed but not balanced by large turbulent forces and accelerations up to 575 mb. From here up to the upper limit of 450 mb, the pressure-gradient and turbulent forces together, weakly opposed by the Coriolis force, produce strong northwestward accelerations.

All three components of the acceleration, $\partial\bar{v}/\partial t$, $\bar{v}\partial\bar{v}/\partial y$ and $\bar{\omega}\partial\bar{v}/\partial p$ (measured in the moving reference frame), contribute to the total about equally in magnitude. The temporal variability would have been substantially smaller but for the rapid changes occurring in the region from 700 to 500 mb. In the frictional or turbulent force, the component due to vertical variation of the eddy momentum flux is several times larger than the horizontal part.

It is encouraging to note that the values of the domain-averaged pressure-gradient force derived hydrostatically from the surface pressure and radiosonde temperature and moisture data are in generally good agreement with the values obtained as a residual from the wind data, except at the top where we have pointed to the questionable wind analysis. No further systematic alteration of the magnitudes of the turbulent forces would improve the agreement significantly.

A detailed picture of the larger accelerations and forces appears in Fig. 4. With a few exceptions needed to indicate the qualitative nature of the balance, only accelerations and forces per unit mass exceeding a magnitude of 2.5×10^{-3} m s^{-2} are shown. Significant effects in the surface boundary layer appear only near and in advance of the SWS as the southeasterly flow decelerates, first from frictional retardation and then from a southeastward pressure-gradient force as the SWS passes. Within the colder air to the northwest there is a commonly observed three-way balance among pressure-gradient, Coriolis and friction forces, with almost no acceleration. Aloft, air entering the system accelerates toward the maximum of v component near 600 mb, about 10 km northwest of the SWS and near the leading edge of the radar echoes. The picture is similar to that shown by Fankhauser (1974). The acceleration is produced mainly by the pressure-gradient force acting toward a geopotential trough. Below 600 mb the turbulent forces act strongly against the existing v component, especially west of the position of its maximum. This effect is sufficient to produce mesoscale deceleration in this region despite a continued northwestward fall of geopotential to a trough roughly 20 km west of the v component maximum. Above 600 mb, maximum and trough approximately coincide along a line west of which the mesoscale flow decelerates despite turbulent forces. In the upper left corner of Fig. 4 we see accelerations and matching pressure-gradient forces, probably resulting from a misrepresentation of a developing circulation to be discussed later.

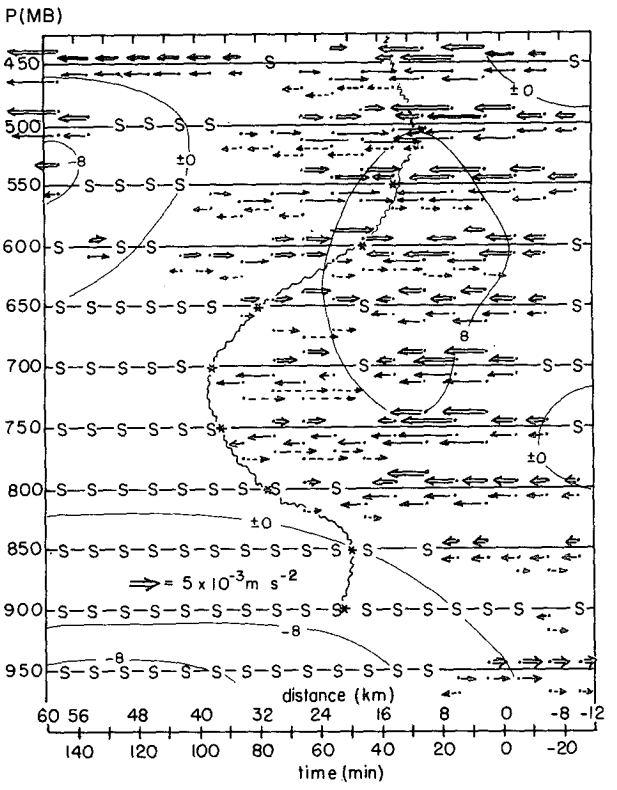

FIG. 4. Detailed presentation of larger accelerations and forces per unit mass in the direction normal to the wind shift line. Plotting convention as in Fig. 3. S indicates that all quantities are relatively small at the grid point. Solid lines are isopleths of the mesoscale $\bar{v}$ component at intervals of 8 m s^{-1}; wavy line is trough line in inferred geopotential field.

It is reassuring that the computed turbulent forces are large only where vigorous convection is present, to judge from the evidence provided by SP. It is most remarkable that the sign of this force, where the magnitude is large, tends to be the same as the sign of the Laplacian of the mesoscale motion, as can be seen from a careful comparison of Figs. 2 and 4. The convective activity seems to be redistributing the v momentum in qualitative accord with the notions of classical diffusion. Though we have made no attempt at a quantitative formulation, the individual balloons seem to represent the turbulent structure well enough to encourage a further attempt at parameterization.

A detailed comparison of horizontal geopotential profiles obtained from Eq. (1), together with those obtained from surface pressure data[1] and hydrostatically from radiosonde temperature and humidity data, is made in Fig. 5. Where "updraft" soundings were present, as discussed by SP, the mesoscale mean virtual temperature was taken as a weighted mean

[1] The surface pressure data were extremely noisy despite our best efforts to correct them. On the whole they did not contradict the profile obtained from the momentum equation.

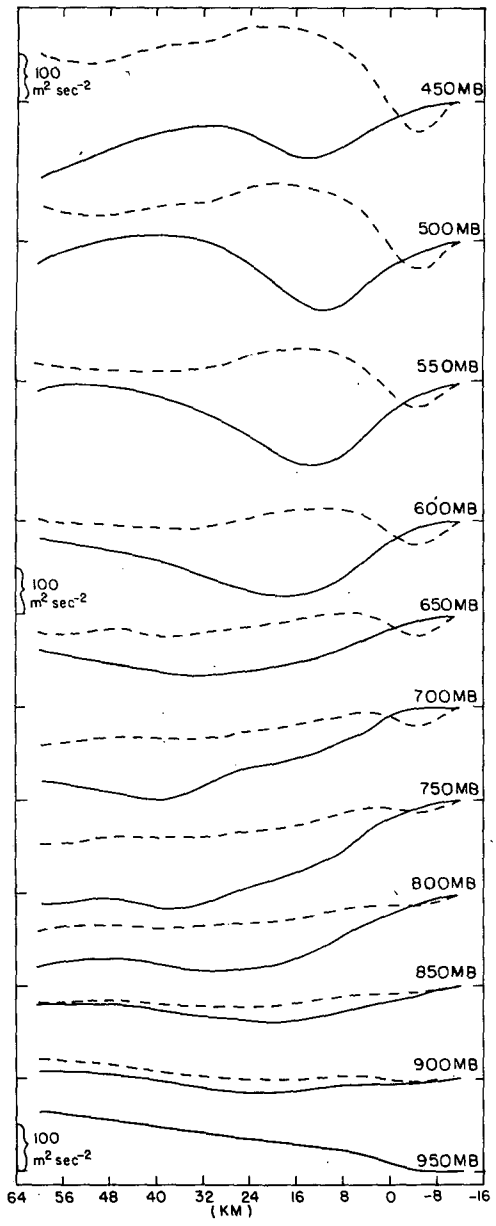

FIG. 5. Profiles of geopotential for individual pressure layers. Solid lines are profiles inferred from momentum equation. Dashed lines are profiles obtained from hydrostatic calculations based on conventional virtual temperature.

of "updraft" and "environmental" values, weighted in a way consistent with the factor of two reduction of turbulent momentum fluxes described earlier. For each layer the two profiles start from a common point 12 km ahead of the SWS. As mentioned earlier, the two profiles are in good agreement 60 km northwest of the SWS; but above the lowest layers the hydrostatic computations show geopotentials larger than the values derived from kinematic considerations, especially in and northwest of the aforementioned trough.

Since this region is characterized by strong radar echoes and heavy precipitation at the ground, we were led to consider the hydrostatic consequence of the presence of liquid water in the air column, relying on the work of Clark and List (1971). On the assumption that the condensed water drops are falling at terminal velocity, the vertical equation of motion can be written

$$(\rho_a+\rho_l)\frac{dw}{dt}=-\frac{\partial p}{\partial z}-(\rho_a+\rho_l)g, \tag{2}$$

where ρ_a and ρ_l are the densities of the air and of the liquid water, respectively. Upon integration between pressure levels p_1, and p_2, Eq. (2) yields, to a high degree of approximation,

$$\Phi_2-\Phi_1=R\bar{T}_v^*\ln\frac{p_1}{p_2}\left(\frac{g}{g+\overline{dw/dt}}\right), \tag{3}$$

where the overbar refers to a mean with respect to the logarithm of pressure through the layer. The "adjusted" mean virtual temperature $\bar{T}_v^*$ is defined by

$$\bar{T}_v^*\equiv\frac{\bar{T}_v}{1+\bar{q}_l}, \tag{4}$$

where $\bar{q}_l$ is the mean liquid-water mixing ratio in the layer.

Measurements from the analyzed field of motion showed that the effect of vertical accelerations was utterly small compared to the uncertainty in the measurement of $\bar{T}_v$ and was thus neglected, i.e., the air column for our purposes can be regarded as being in hydrostatic equilibrium despite the presence of strong mesoscale vertical motions.

The hydrostatic profiles (Φ_H) shown in Fig. 5 were computed, in effect, with $\bar{q}_l=0$. We can assume that the discrepancy between the profiles of Φ_H and Φ_K (derived from the momentum budget) is due to the neglected liquid water. We are saying in effect that the value of $\bar{T}_v^*$ in Eq. (3) is that implied by the geopotential profiles obtained from momentum considerations, or

$$\Phi_{K2}-\Phi_{K1}=R\bar{T}_v^*\ln\frac{p_1}{p_2}, \tag{5}$$

while

$$\Phi_{H2}-\Phi_{H1}=R\bar{T}_v\ln\frac{p_1}{p_2}. \tag{6}$$

From (4), (5) and (6) we obtain an inferred value of $\bar{q}_l$ as a residual from

$$\bar{q}_l=\frac{\Phi_{H2}-\Phi_{H1}}{\Phi_{K2}-\Phi_{K1}}-1. \tag{7}$$

The profile of $\bar{q}_l$ for the entire depth from the surface to 450 mb, from 12 km southeast to 60 km northwest

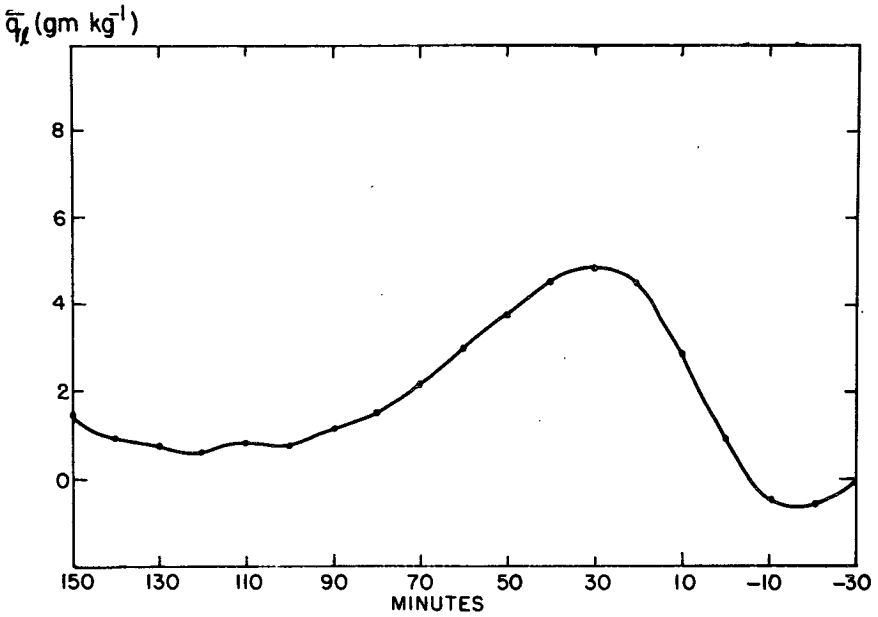

FIG. 6. Liquid water load, averaged from the surface to 450 mb, inferred from the difference between geopotential profiles presented in Fig. 5.

of the SWS, is given in Fig. 6. In view of the available precipitation and radar data this profile seems reasonable, although the maximum of $\bar{q}_l$ should probably lie farther northwest. The detailed pattern for individual 50 mb layers, however, did not appear quantitatively realistic, so we have evidently found the limit of reliability of the observations. It seems safe to assert, however, that the effect of liquid-water load is a significant factor in the geopotential field associated with mesoscale storms.

4. Temporal evolution of the storm structure

Of the patterns of temporal change of the several variables in the moving coordinate system, the most striking and extensive was in the v component of wind from about 20 to 60 km northwest of the SWS (Fig. 7). The observations in this region, made mainly between about 2000 and 2200 CST, show the systematic growth of a circulation of northwesterlies between 850 and 700 mb, capped by southeasterlies of maximum intensity around 550 mb.

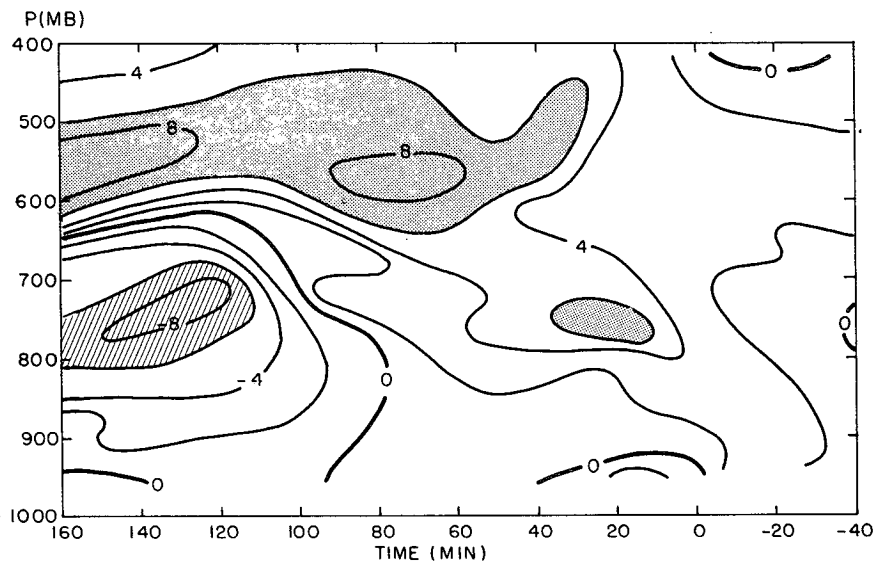

FIG. 7. Rate of change of the mesoscale $\bar{v}$ component of wind in the coordinate system moving with the surface wind shift line. Isopleths are at intervals of 2 m s^{-1} h^{-1}.

Time variations of individual balloon v-component values, on which the analysis is based, are shown in Fig. 8. There can be little doubt of the reality of this development, in which the reversal of sign of the developing flow lies near the base of a thick and extensive layer of middle cloud (to judge from surface observations) extending northwestward from the main updraft. The extrapolation of these trends to 2000 CST, prior to the time of the observations used to establish them, leads to the probable error in the flow depicted in Fig. 2 beyond about 40 km northwest of the SWS, as mentioned earlier. The implication is that these trends in fact became established after 2000 CST and were not a characteristic of the system during its entire life history.

Substantial precipitation fell from this middle cloud deck, probably into unsaturated air below. It seems likely on the basis of mass conservation that a substantial mesoscale downdraft was simultaneously developing beyond the northwestward limits of our observations, driven by evaporative cooling in the manner proposed by Zipser (1969) as typical of many tropical convective systems. Some evidence of evaporative cooling at the edge of the observational domain was presented by SP. This inferred downdraft is, of course, entirely separate from the strong downdraft at the leading edge of the system, which presumably developed earlier and which SP attributed to evaporation of the tops of vigorous cumulus growing from the surface boundary layer. The subsequent downdraft to the northwest has no clear association with events in the surface boundary layer.

The vertical cross sections from the NSSL radar add to our view of the evolution of the system in time (Fig. 9). Initially (1730 CST), just prior to the entry of the front into the surface network, we see a single cell about 10 km wide and about 15 km northwest of the SWS. It drifts slowly southeastward relative to the earth but loses ground to the more rapidly advancing surface front. At 1815 CST a new cell appears near 5 km elevation about 15 km northwest of the SWS, developing quickly as the old cell

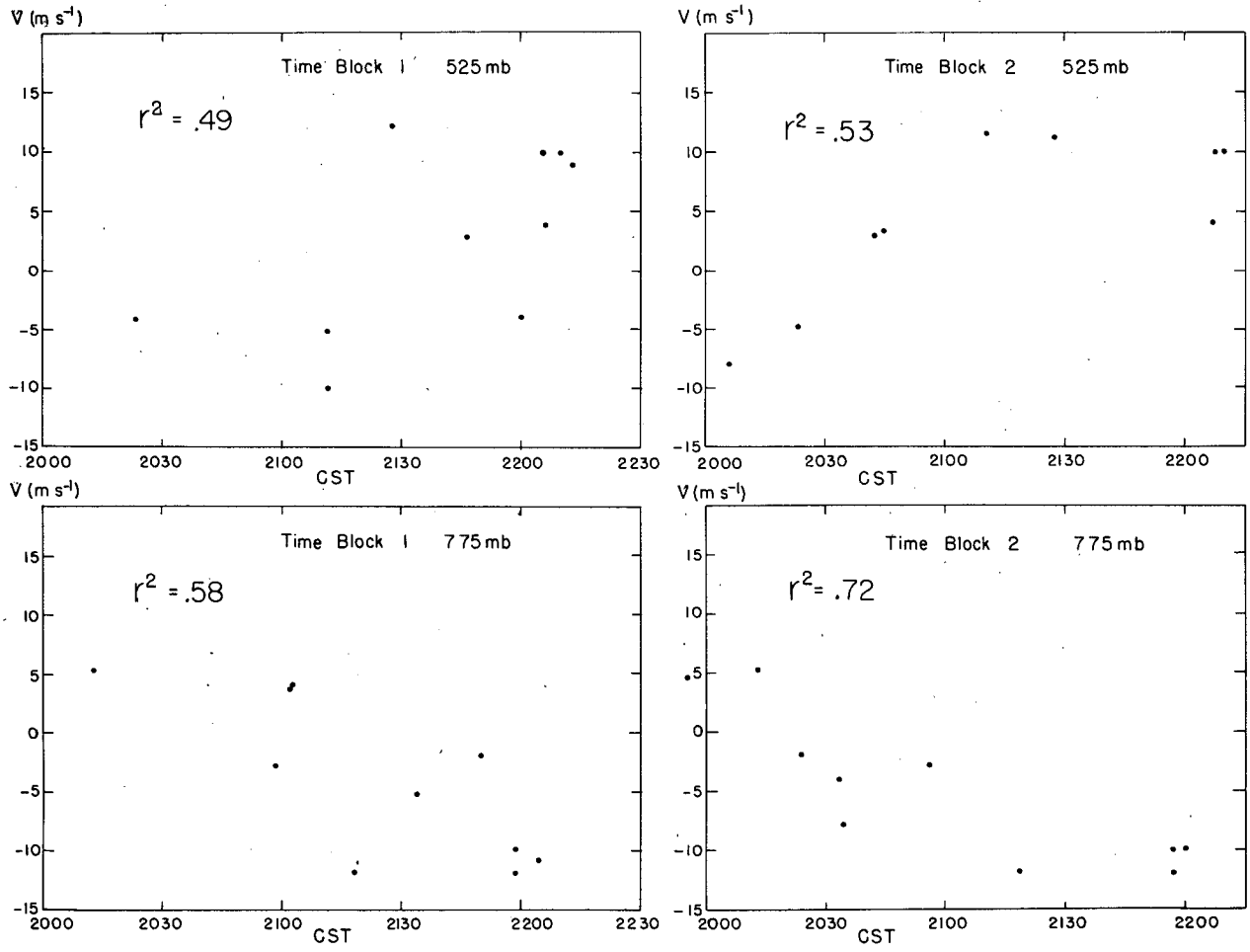

FIG. 8. Sample plots of v component observed by individual balloons within certain time blocks and pressure layers. The value of r^2 is the percent of variance explained by the linear regression lines (not shown) fitted to the data.

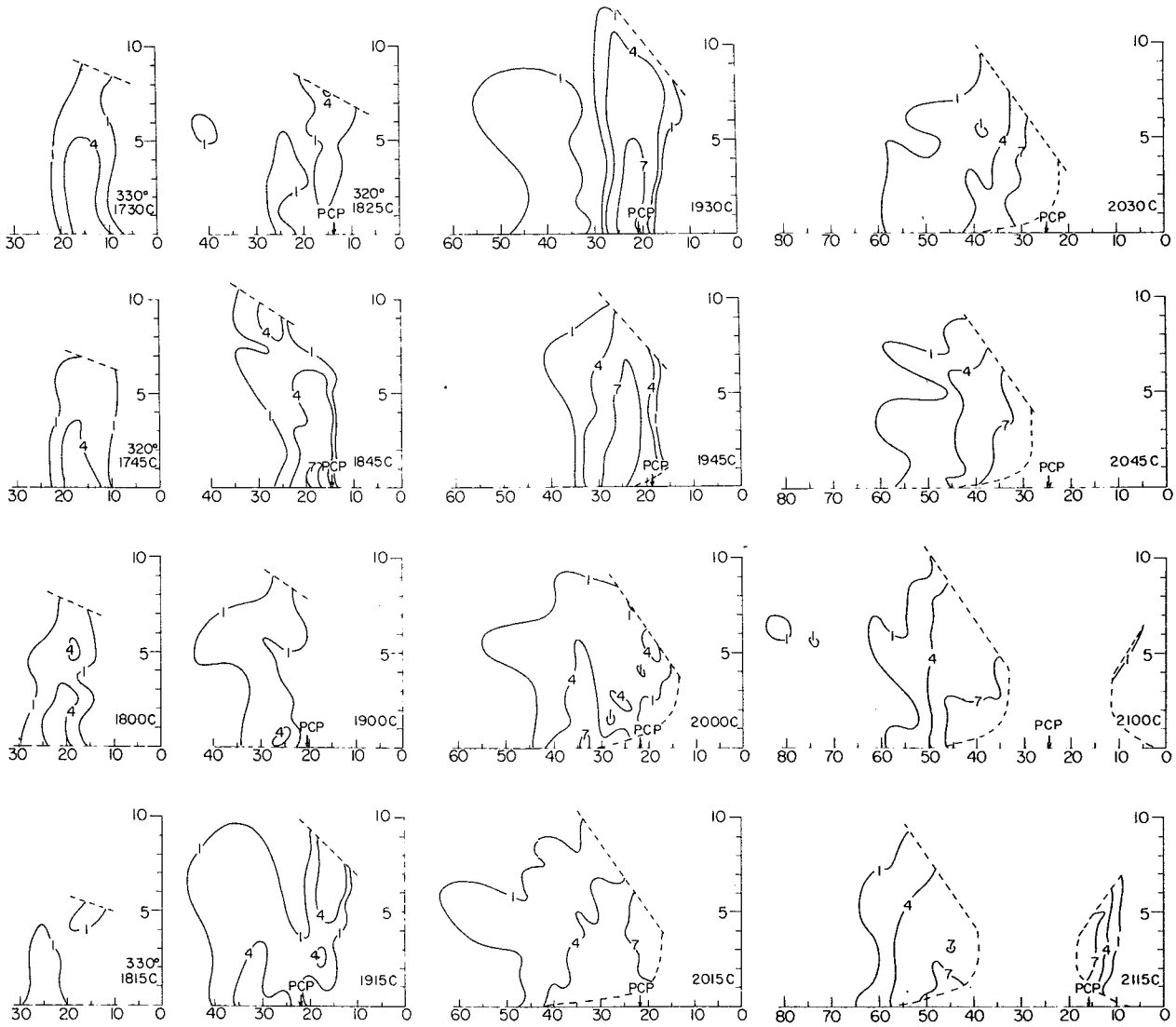

FIG. 9. Vertical cross sections of radar echoes observed by the NSSL radar, at intervals of 15 min (except around 1825 CST), along azimuth 325° (except where noted). Abscissa and ordinate are in kilometers, with zero indicating the position of the surface wind shift. The point of onset of precipitation at the surface, when known, is indicated by PCP. Isopleths 1, 4 and 7 represent intensities of 20, 37 and 62 dBz, respectively. The dashed lines indicate the limit of radar visibility due to ground clutter and limited elevation angle.

dissipates. This process is seen to repeat, new cells appearing in approximately the same location relative to the SWS at 1915, 2000 and presumably at 2100 CST (the last lying largely in the ground clutter in the unobserved cone above the maximum radar elevation angle).

Examination of the PPI presentation shows that these cells were not randomly distributed, drifting laterally into the plane of the section, but rather were members of lines that generated at the nearly regular intervals indicated above. We suggest that this interval of 45 min to 1 h corresponds to the effective lifetime of the individual convective element, during which its circulation suppresses other nearby convective activity. Initially the lines were not solid, so that the azimuth of the section had to be altered slightly to intercept a cell. Later the lines were relatively continuous.

Note further that the debris from each cell tends to persist more strongly than that of its predecessor, so that, finally (2115 CST), echoes of at least moderate intensity span a distance of about 45 km normal to the front. After this time only PPI scans at zero-elevation angle were available. They indicated that the echo area tended to broaden further and to lose the strong reflectivity gradient characteristic of the leading edges, while moving little as a whole. Surface observations in northwestern Oklahoma indicated the *beginning* of rain and thunder 8–13 h after passage of the surface front!

This information suggested to us the highly speculative view of the evolution of the system sketched

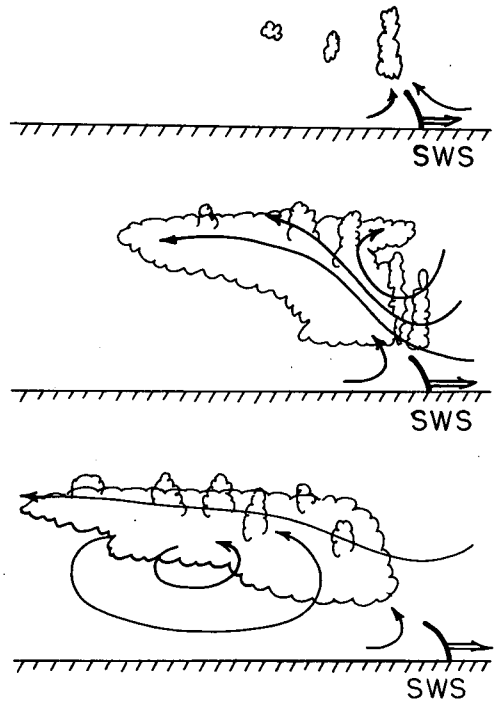

FIG. 10. Schematic evolution of convective mesosystem: top, inception phase; middle, mature phase; bottom, dying stage.

in Fig. 10. Initially there is no substantial mesoscale circulation aloft, the only active convection being closely associated with strong low-level convergence near the SWS. Some debris from previous active clouds lies to the northwest. Later the SWS is still triggering active convection, but a pronounced mesoscale updraft–downdraft couplet has developed. The downdraft aloft over the SWS is driven by evaporative cooling at the tops of growing cumulus; and the updraft is driven by latent heat release in an extensive cloud mass to the northwest, the latter aided toward saturation by the accumulation of previous debris. This middle stage is the one to which the observations in our case principally refer. In the final stage, the main cloud mass is very extensive but not connected to the SWS. The circulation gradually runs down because of the stabilizing and drying effect of the recycled air. The entire life history spans something on the order of 10 h.

The system as a whole is not simply a large, quasi-steady cumulonimbus cloud and is probably not to be understood in terms of thermal buoyancy (however adorned with added physical effects). Cumulus convection, however, plays a key role once initiated by low-level convergence. For example, divergence of eddy flux of momentum, evidently associated with convection, constitutes an important horizontal force; and convection provides the cloud water for evaporation needed to drive the main downdraft. The major cloud mass associated with the mesoscale updraft, though slightly stable hydrostatically, contains embedded active convective elements, probably small masses of air of boundary-layer origin which by chance escaped the main mixing process on entry into the storm and thus retained their anomalously high value of equivalent potential temperature. In other cases, but not in this one, vigorous convective elements embedded within (or at the edge of) the mesoscale cloud mass may produce tornadoes and other severe weather phenomena.

5. Concluding comments

We suggest that, with few exceptions, long-lasting "convective" storms, whether of frontal, air mass or squall line type, contain as eclectic elements not only vigorous cumulus activity but also a vigorous associated mesoscale circulation organized in a way generally similar to what we see in this case. The synoptic-scale structure dictates the particular character of the mesoscale system. In this case the large-scale vertical wind shear was relatively small and the mesosystem developed in a direction downshear (mainly ageostrophic) from the intense convection, nearly transverse to the line of storms.

In other cases there may be strong large-scale shear in a direction normal to the direction of propagation of a limited area of deep convection. The associated mesosystem may then be long and narrow, elongated in the direction of the shear.

Yet other possibilities can be imagined in other synoptic environments. We hope they will be documented by future field programs. In the meantime it may be fruitful to examine the large existing archive of radar film and conventional surface observations with these models in mind.

Acknowledgments. The authors are grateful to David I. Katz, Judi Stokes and Razia Ahmad for their assistance in the preparation and analysis of data. This research was supported by the Atmospheric Sciences Section, National Science Foundation, under Grant DES74-24405.

REFERENCES

Clark, T. L., and R. List, 1971: Dynamics of a falling particle zone. *J. Atmos. Sci.*, **28**, 718–727.

Fankhauser, J. C., 1974: The derivation of consistent fields of wind and geopotential height from mesoscale rawinsonde data. *J. Appl. Meteor.*, **13**, 637–646.

Sanders, F., and R. J. Paine, 1975: The structure and thermodynamics of an intense mesoscale convective storm in Oklahoma. *J. Atmos. Sci.*, **32**, 1563–1579.

Zipser, E. J., 1969: The role of organized unsaturated convective downdrafts in the structure and rapid decay of an equatorial disturbance. *J. Appl. Meteor.*, **8**, 799–814.